#### **Research Article**

Hanbo Zhu, Jibing Deng, Mei-Ling Zhuang\*, Chuanzhi Sun, Li Gao, Yuefeng Shao, Mingsen Wang, Youzhi Wang, Yao-Rong Dong, and Lei Tong

# Numerical investigations on constitutive model parameters of HRB400 and HTRB600 steel bars based on tensile and fatigue tests

https://doi.org/10.1515/rams-2023-0186 received August 02, 2023; accepted January 29, 2024

Abstract: In recent years, HRB400 and HTRB600 steel bars have become the mainstream standard reinforcing steel used in concrete structures in China. However, significant controversy still exists regarding the selection of material constitutive models and the determination of model parameters for buckling, fatigue, hysteresis, and other material characteristics. In this article, an automated process of multi-parameter calculation of the constitutive model for reinforcing steel - simulation accuracy evaluation of the constitutive model - selection of the constitutive model of reinforcing steel is established based on the hybrid programming method using MATLAB and OpenSees software. First, tensile and low-cycle fatigue tests were carried out on HRB400 and HTRB600 steel bars. Second, based on the constitutive model in OpenSees software and the skeleton curve and characteristics such as yielding, fatigue, and hysteresis, the constitutive model parameters of HRB400

and HTRB600 steel bars are determined using indirect and direct fitting methods. Finally, the five similarity parameters of the simulated normalized cumulative hysteretic energy dissipation coefficient are compared with the test results. The results indicate that the simulation accuracy of the Reinforcing Steel model exceeds 72%, which is higher than other four models, making it the best choice for reinforcing steel in numerical simulation.

**Keywords:** low-cycle fatigue property, constitutive model of reinforcing steel, fatigue parameters, indirect method, direct method

### 1 Introduction

The process and performance of steel bars with tensile strengths ranging from 300 to 600 MPa are covered in Chinese current codes [1,2]. The two parameter values of the yield strength and ultimate strain are defined in the codes, while the other parameters are unspecified in the codes. The mechanical properties of each strength class of reinforcing steel in terms of the fundamental parameters (modulus of elasticity, yield strength, ultimate strain, etc.), [3–5], residual stresses [6,7], fatigue effects [8], and buckling effects [9] were investigated. Then, the mechanical behavior of reinforcing bars was simulated using simple models such as bifold, trifold, and Ramberg-Osgood [10]. Fernandez et al. [11] used X-ray diffraction techniques to reveal the fatigue damage mechanism from the perspective of microstructural changes and successfully predicted the mechanical property parameters of steel bars. Abdalla and Hawileh [12] and Chou et al. [13] used artificial neural networks to obtain an effective prediction method for the mechanical property parameters of steel bars based on a large number of experimental results. However, the above methods for calculating steel performance parameters require a large amount of test data, which are difficult to model mathematically.

**Hanbo Zhu, Chuanzhi Sun, Li Gao:** School of Civil Engineering and Architecture, Suqian College, Suqian, 223800, China; Jiangsu Province Engineering Research Center of Prefabricated Building and Intelligent Construction, Suqian College, Suqian, 223800, China

**Jibing Deng:** China Construction Fifth Engineering Bureau Co., Ltd., Changsha, 410004, China

**Yuefeng Shao:** College of Civil Engineering and Architecture, Jiangsu University of Science and Technology, Zhenjiang, 212100, China **Mingsen Wang:** Water Resources Research Institute of Shandong Province, Jinan, 250013, China

Youzhi Wang: School of Civil Engineering, Shandong University, Jinan, 250061, China

**Yao-Rong Dong:** School of Civil Engineering, Xi'an University of Architecture and Technology, Xi'an 710055, China

**Lei Tong:** Suqian City Urban Construction Investment (Group) Co., Ltd., Suqian, 223800, China

<sup>\*</sup> Corresponding author: Mei-Ling Zhuang, Water Resources Research Institute of Shandong Province, Jinan, 250013, China; School of Transportation and Civil Engineering, Nantong University, Nantong, 226019, China; School of Civil Engineering, Shandong University, Jinan, 250061, China, e-mail: ml\_zhuang99@163.com

In recent years, the open-source software OpenSees has been promoted and applied in the seismic analysis of reinforced concrete structures. To better determine the performance parameters of reinforcing steel and improve the simulation accuracy of reinforcement steel in the admissibility process, scholars have used the rich constitutive model relationships in OpenSees software to determine the model parameters with a small amount of test data and display functions, then they simulate the mechanical properties of the reinforcement steel. Zhang et al. [14], Xu et al. [15], and Gao et al. [16] calculated the fatigue parameters and predicted the fatigue life by Coffin-Manson relationship for HRB400 and HTRB600E grade steel bars, respectively. Han et al. [17] studied the fatigue effect of ultra-high strength considering the buckling effect. Till date, the methods of fitting model parameters with display functions combined with experimental results have all focused on the study of fatigue and buckling effects of steel bars, which are not summarized and generalized. At the same time, most of the constitutive models in OpenSees are very complex, which cannot be expressed directly by the display. Therefore, it is very difficult to determine the model parameters.

In recent years, HRB400 and HTRB600 steel bars have become the mainstream standard reinforcing steel used in concrete structures in China. There is a unified understanding of the actual strength and ductility of HRB400 and HTRB600 steel bars. However, significant controversy still exists regarding the selection of material constitutive models and the determination of model parameters for buckling, fatigue, hysteresis, and other material characteristics. The refinement and complexity of existing steel bar constitutive models are constantly increasing. This has caused great difficulties for researchers to choose appropriate models and determine model parameters, and correctly simulate the hysteresis curve of steel bars in experiments. For this purpose, static tensile tests and low cycle fatigue tests were conducted on domestically produced HRB400 and HTRB600 steel bars in China. To solve the above problems, HRB400 and HTRB600 steel bars are taken as research objects and static tensile tests and low cycle fatigue tests were conducted on them. In OpenSees software, the constitutive model of reinforcing steel is chosen. Considering energy dissipation capacity, deformation characteristics, stiffness, and strength degradation, the constitutive model parameters of HRB400 and HTRB600 steel bars are determined using indirect and direct fitting methods according to skeleton curves and buckling, fatigue, hysteresis, and other characteristics. The effectiveness and accuracy of the constitutive model parameter determination methods for HRB400 and HTRB600 steel bars were verified through comparison of simulation and experimental results.

# 2 Monotonic tensile and low-cycle fatigue testing

#### 2.1 Static tensile test

Reinforced concrete structures often experience uniaxial stress conditions during earthquakes. This article focuses on discussing the stress-strain relationship of steel bars under uniaxial tension and compression. The engineering stress-strain curves presented here are intended to be obtained through unidirectional tensile or cyclic tests conducted on standard-grade steel bars. To obtain the basic mechanical parameters of HRB400 and HTRB600 steel bars, static tensile tests were conducted. Three specimens of each type of steel bars were taken in the test. The diameter of the specimens was 18 mm. The length of the specimens was 400 mm. The tensile test was performed on the 1000HDS electronic universal hydraulic testing machine acc test method in the code [18]. Figure 1 shows the tensile test setup. The stress-strain curves of steel bars were obtained through tensile testing using a universal testing machine. The strain was accurately measured using an extensometer. The specific procedure can be found in the code [18]. The stress–strain curves of HRB400 and HTRB600 steel bars are illustrated in Figure 2. The static tensile properties of steel bars are listed in Table 1. The yield strengths of HRB400 and HTRB600 steel bars were greater than the specification requirement values in ref. [19].

### 2.2 Fatigue test

The low-cycle fatigue properties of HRB400 and HTRB600 steel bars were investigated by the tension-compression



Figure 1: Test setup.

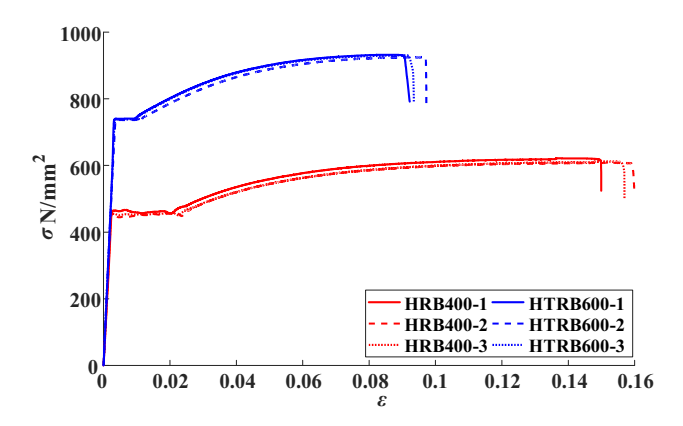


**Figure 2:** Stress–strain curves of HRB400 and HTRB600 grade reinforcement.

constant strain amplitude tests [20,21]. The strain amplitudes are set as 1.0, 1.2, 1.6, 1.8, and 2.0%. Figure 3 gives the details of the steel bar specimens. Two specimens of each type of steel bar were taken in the test. The specimens were numbered SJQ-i-j, where SJ denotes the specimen, Q represents the steel strength, i denotes the loading strain amplitude, and j denotes the number of the same loading condition. SJ400-1.2%-1 denotes the first HRB400 steel bar specimen under 1.2% strain amplitude loading. The MTS 322 testing system (Figure 4) was applied in the test. The extensometer had a gauge length of 50 mm and a range of 20 mm. The loading frequency was 1 Hz. The loading diagram is illustrated in Figure 5. The fatigue test stress—strain curves of HRB400 and HTRB600 steel bars are as described in Figure 6.



Figure 4: Loading system.

The stress-strain curves of HRB400 and HTRB600 steel bars under different strain amplitude loading conditions are shown in Figure 6. The peak of the skeleton curve of the specimen decreased after the first cycle, and then the decrease in peak of the subsequent cycles gradually increased until the specimen failed. Similarly, with the load application, the loading curve pinching phenomenon gradually increased, the energy dissipation capacity decreased, the hysteresis loop became flattered, and the flattening process gradually increased until the specimen failed. Comparing the test data of specimens with different strain amplitudes, it was found

Table 1: Static tensile properties of steel bars

Mechanical properties of reinforcing steel index		HR	B400			Н	RB600	
	1	2	3	Average	1	2	3	Average
Yield strength $\sigma_{\rm sv}$ (MPa)	458.74	449.38	451.66	453.26	740.29	736.10	739.24	738.55
Strain at yield onset $\varepsilon_{sy}$ (10 <sup>-3</sup> )	2.42	2.20	2.26	2.29	3.67	3.78	3.70	3.72
Modulus of elasticity $E_s$ (GPa)	189.56	204.26	199.85	197.89	201.71	194.74	199.80	198.75
Reinforced starting point strain $\varepsilon_{sh}$ (10 <sup>-3</sup> )	20.17	23.48	24.53	22.73	10.38	11.54	12.40	11.44
Initial modulus of elasticity of reinforced section $E_{sh}$ (MPa)	48.32	26.29	27.76	34.12	36.72	64.16	12.56	37.81
Peak strength $\sigma_{sp}$ (MPa)	622.02	607.52	611.86	613.80	932.09	924.94	930.31	929.11
Peak strain $\varepsilon_{\rm sp}$ (10 <sup>-3</sup> )	136.32	152.67	147.77	145.59	86.35	93.82	88.22	89.46

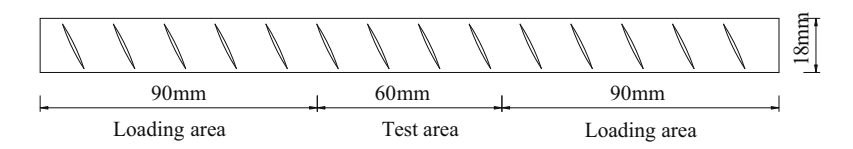


Figure 3: Dimensional drawing of the specimen.

4 — Hanbo Zhu *et al.* DE GRUYTER



Figure 5: The loading diagram.

that the specimens under large displacement amplitudes had a sparser distribution of the cyclic curve, (*i.e.*, the larger the strain amplitude), each cycle caused more reduction in the bearing capacity of the specimen, and the number of cycles was less when the specimen failed. This is because as the strain amplitude increases, the stress concentration of the specimen increases, the crack extension intensifies, the accumulation of plastic deformation accelerates, and the microstructural changes become more pronounced, thus accelerating the strength degradation of the specimen.

### 3 Rebar model in OpenSees software

A large number of constitutive models for reinforcing steel are provided in OpenSees software [22], such as Steel01

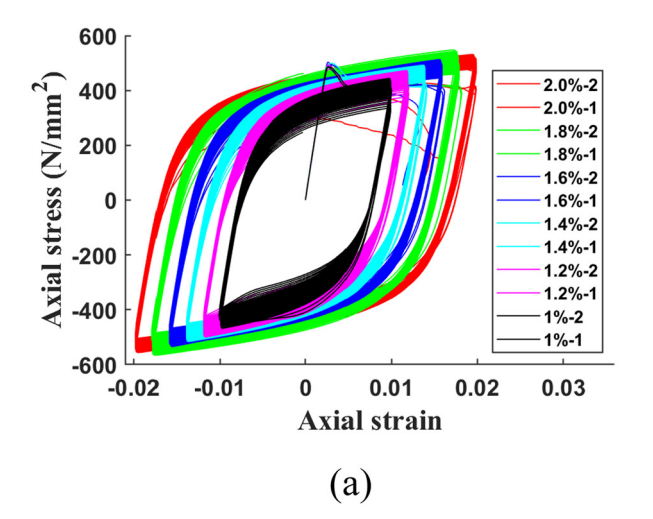
model, Steel02 model, Steel4 model, and Reinforcing Steel model. Table 2 summarizes a comparison of different constitutive models of reinforcement steel. Steel4 model and Reinforcing Steel model are more comprehensive and can be used for the simulation of low-cycle fatigue under reciprocal loading conditions. Skeleton curves and hysteretic curves are segmented linear models, which can simulate the declining section curve of reinforcing steel better, although the simulation effect of fatigue property is not good. Among these nine types of constitutive models for reinforcing steel, the Dodd-Restrepo model, Menegotto-Pinto model, and Coffin-Manson model have a simple functional form, and the skeleton curve, hysteresis effect, and fatigue effect function parameters can be fitted directly according to the model functions, respectively. The specific function and parameter meanings of the three rebar property models are as follows.

### 3.1 Dodd-Restrepo model

The C-M model [23–25] is the full functional expression of the Dodd-Restrepo model. The functional relationship between the strain  $\varepsilon_s$  and stress  $\sigma_s$  of reinforcing steel is described in Figure 7 and Eq. (1).

$$\sigma_{s} = \begin{cases}
E_{s}\varepsilon_{s}, & \varepsilon_{s} \leq \varepsilon_{sy} \\
\sigma_{sy}, & \varepsilon_{sy} \leq \varepsilon_{s} \leq \varepsilon_{sh} \\
\sigma_{su} + (\sigma_{y} & \varepsilon_{sh} \leq \varepsilon_{s} \leq \varepsilon_{su}, \\
- \sigma_{su})|(\varepsilon_{su} - \varepsilon_{s})/(\varepsilon_{su} - \varepsilon_{sh})|^{p},
\end{cases} (1)$$

where  $E_s$  is the modulus of elasticity of reinforcing steel [26];  $\varepsilon_{sv}$  is the yield strain;  $\sigma_{sv}$  is the yield stress;  $\varepsilon_{sh}$  is the



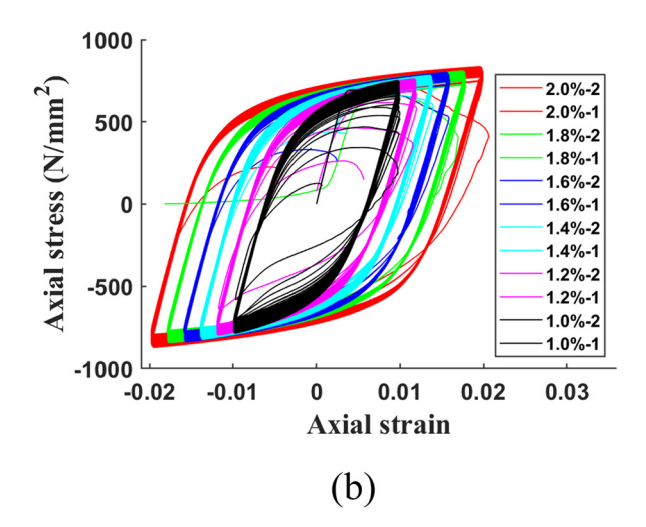


Figure 6: Stress-strain curve for fatigue test of steel bars. (a) HRB400 steel bars. (b) HTRB600 steel bars.

Table 2: Constitutive model for reinforcing steel in OpenSees software

Constitutive model	Skeleton curve model	Hysteresis model	is model	Fatigue model	Flexion model	Is there	Has asymmetry
		Random hardening	Isotropic hardening			initial stress?	been considered?
Steel01	Bilinear model	Bilinear model	Stanton–Niven model	1	1	No	No
Steel02	Menegotto–Pinto model	Menegotto–Pinto model	Stanton–Niven model			Yes	No
Steel4	Menegotto–Pinto model	Menegotto–Pinto model	Adam Zsarnóczay model	Strength discounting model		Yes	Yes
Hysteretic	Trilinear model	A trilinear model considering li effects of energy and intensity	A trilinear model considering linear cumulative damage effects of energy and intensity			0 N	Yes
Pinching4	Quadratic linear model	A trilinear mod effects of ducti	g the cumulative damage and strength			0 N	Yes
Reinforcing Steel	Dodd-Restrepo model	Menegotto-Pinto model	Chang–Mander model	Coffin–Manson fatique model	Gomes–Appleton model/ Dhakal–Maekawa model	No No	No
Dodd-Restrepo Steel	Dodd-Restrepo model	Dodd-Restrepo model			_	No	No
SteelMPF	Menegotto–Pinto model	Menegotto–Pinto model	Stanton–Niven Model			No No	No
Ramberg–Osgood Steel Ramberg–Osgood model	Ramberg–Osgood model	Ramberg–Osgood model		1	1	No	No

Note: 1. The hybrid hardening model is a mixture of follower hardening and isotropic hardening. 2. The Stanton-Niven model obtains an isotropic hardening model by adjusting the yield point. 3. Dodd-Restrepo is an incremental expression and Ramberg-Osgood is an implicit expression.

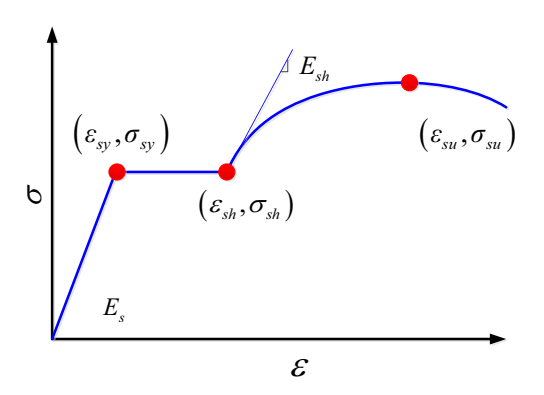


Figure 7: Monotonic loading curve for steel bars.

maximum strain of the yield segment, taking values between 1 and 3%;  $\sigma_{su}$  is the ultimate stress;  $\varepsilon_{su}$  is the ultimate strain, taking values between 10 and 18% [27,28].

The index P is defined as

$$p = E_{\rm sh} \frac{\varepsilon_{\rm su} - \varepsilon_{\rm sh}}{\sigma_{\rm su} - \sigma_{\rm sv}},\tag{2}$$

where  $E_{\rm sh}$  is the initial modulus of elasticity of the hardened section [24].

$$E_{\rm sh} = 0.02E_{\rm s}(1 \pm 20\%).$$
 (3)

Tangential modulus of the hardened branch  $E_t$  can be expressed as follows:

$$E_{\rm t} = E_{\rm sh} \left| \frac{\sigma_{\rm su} - \sigma_{\rm s}}{\sigma_{\rm su} - \sigma_{\rm sy}} \right|^{1-1/p}.$$
 (4)

### 3.2 Menegotto-Pinto model

The functional expression of the Menegotto-Pinto model [29,30] is

$$\sigma_{\rm s}^* = b\varepsilon_{\rm s}^* + \frac{(1-b)\varepsilon_{\rm s}^*}{(1+\varepsilon_{\rm s}^{*R})^{\frac{1}{R}}},\tag{5}$$

where r is the cyclic curve shape parameter; b is the asymptotic initial elastic modulus and hardened modulus ratio;  $f_{\rm s}^*$  and  $\varepsilon_{\rm s}^*$  are the normalized reinforcement stress and strain, respectively, which can be calculated using Eqs. (6)–(8).

$$b = \frac{E_{\rm ss}}{E_{\rm s0}},\tag{6}$$

$$\varepsilon_{\rm s}^* = \frac{\varepsilon_{\rm s} - \varepsilon_{\rm sr}^n}{\varepsilon_{\rm sy}^{(n+1)} - \varepsilon_{\rm sr}^n},\tag{7}$$

$$\sigma_{\rm S}^* = \frac{\sigma_{\rm S} - \sigma_{\rm Sr}^n}{\sigma_{\rm SV}^{(n+1)} - \sigma_{\rm Sr}^n},\tag{8}$$

where  $E_{s0}$  and  $E_{ss}$  are the initial tangential modulus and hardening modulus of the half cycle under reciprocal loading, respectively;  $\varepsilon_{sr}^n$  and  $\sigma_{sr}^n$  are the strains and stresses corresponding to the nth half cycle and the (n+1)th half cycle intersection;  $\varepsilon_{sr}^{(n+1)}$  and  $\sigma_{sr}^{(n+1)}$  are the strains and stresses corresponding to the (n+1)th half cycle yield point; for the (n+1)th half-cycle, the unloading point is the intersection of two asymptotes of  $(\varepsilon_{sr}^n, \sigma_{sr}^n)$ , and the yield point  $(\varepsilon_{sr}^{(n+1)}, \sigma_{sr}^{(n+1)})$ ; and the yield stress  $\sigma_{sy}^1$  and  $\sigma_{sy}^n, \varepsilon_{sy}^n, \varepsilon_{sr}^n$  and b are known to obtain  $\sigma_{sr}^{n+1}$  for the next cycle and  $\varepsilon_{sy}^{n+1}$  for the next cycle by  $\sigma_{sr}^n$  and  $\sigma_{sy}^n$ , and the initial tangential stiffness  $E_{s0}$ .

The (n+1)th half-cycle curve shape parameter  $R_{n+1}$  can be expressed as

$$R_{n+1} = R_0 \left[ 1 - \frac{A_1 \xi_n}{A_2 + \xi_n} \right], \tag{9}$$

where  $R_0$  is the initial curve shape parameter;  $A_1$  and  $A_2$  are the cycle parameters that affect the cyclic properties of the material; and  $\xi_n$  is the speciated plastic deformation of the nth half-cycle, obtained by normalizing the strain  $\varepsilon_{\rm sy}$  at the initial yield point.

$$\xi_n = (\varepsilon_{\rm sr}^n - \varepsilon_{\rm sv}^n)/\varepsilon_{\rm sv},\tag{10}$$

where  $\varepsilon_{sr}^n$  and  $\varepsilon_{sy}^n$  are the initial unloading strain and yield strain for the *n*th half cycle, respectively.

Mander corrects the curve shape parameter R without considering the cycle period [31]:

$$R = \varepsilon_{\rm SV}^{R_1} R_2 (1 - R_3 (\varepsilon_{\rm S} - \varepsilon_{\rm SV})), \tag{11}$$

where  $R_1$ ,  $R_2$ , and  $R_3$  are the parameters to be determined for the shape parameters.

The shape parameter of the curve considering cycle time  $R_{n+1}$  is applicable for Steel2, Steel4, and SteelMPF models. The shape parameter of the curve without considering the cycle time  $R_{n+1}$  is applicable to Reinforcing Steel model.

#### 3.3 Coffin-Manson model

Without considering the influence of elastic strain on the fatigue life, the fatigue damage effect  $D_{\rm f}$  for the Coffin–Manson model considering fatigue effects under any loading path is:

$$D_{\rm f} = \sum \left(\frac{\varepsilon_{\rm sp}}{C_{\rm f}}\right)^{\frac{1}{\alpha}},\tag{12}$$

F 4

where the damage effect  $D_f$  takes values between 0 and 1;  $C_{\rm f}$  is the fatigue coefficient;  $\alpha$  is the fatigue index coefficient; and  $\varepsilon_{\rm sp}$  is the plastic part of the strain;  $\varepsilon_{\rm sp}$  =  $\varepsilon_{\rm s}$  - $\sigma_{sy}/E_s,~\epsilon_{sp}$  is the total strain of reinforcement steel, and  $\sigma_{sv}$  is the yield stress of reinforcement steel.

Considering the damage effect, the strength degradation effect factor  $\phi_{\rm SR}$  can be expressed as Eq. (13) based on the Miner's linear law.

$$\phi_{\rm SR} = \sum \left[ \frac{\varepsilon_{\rm sp}}{C_{\rm d}} \right]^{\frac{1}{\alpha}},\tag{13}$$

where  $C_d$  is the strength degradation factor.

In the process of constant strain amplitude loading, Egs. (12) and (13) can be rewritten as

$$D_{\rm f} = N_{\rm h} \left( \frac{\varepsilon_{\rm sp}}{C_{\rm f}} \right)^{\frac{1}{\alpha}},\tag{14}$$

$$\phi_{\rm SR} = (N_{\rm h} - 2) \left( \frac{\varepsilon_{\rm sp}}{C_{\rm d}} \right)^{\frac{1}{\alpha}}, \tag{15}$$

where  $N_h$  is the number of half-cycle periods and  $C_f$ ,  $C_d$ , and  $\alpha$  are the parameters to be determined; the suggested values of fatigue parameters for HRB400 and HTRB600 steel bars are given in the previous studies [32,33].

Based on the functional expressions of the three abovementioned models, constitutive model parameters can be directly fitted to describe the skeleton curve, hysteresis effect, and fatigue effect of a specific steel bar. In addition, the Reinforcing Steel model considers the buckling effect of reinforcing steel using the two fatigue models, Gomes-Appleton [34] and Dhakal-Maekawa. The parameter values of the two fatigue models are related to the parameters of reinforced concrete columns.

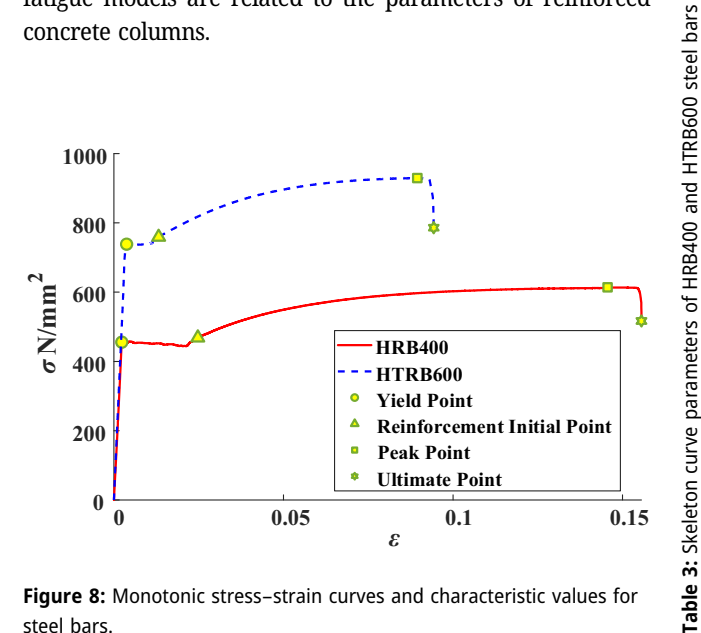


Figure 8: Monotonic stress-strain curves and characteristic values for steel bars.

teel bars	$\varepsilon_{\rm sy} \ (10^{-3})$	σ <sub>sy</sub> (MPa)	$\mathcal{E}_{\rm Si}~(10^{-2})$	σ <sub>si</sub> (MPa)	$\varepsilon_{\rm sp} \; (10^{-1})$	σ <sub>sp</sub> (MPa)	$\varepsilon_{\rm su} \ (10^{-1})$	σ <sub>su</sub> (MPa)	b (10 <sup>-2</sup> )	E <sub>sh</sub> (MPa)	E <sub>s</sub> (10 <sup>5</sup> MPa)	$l_{yp}$
1RB400	2.3	453	2.27	454	1.46	614	1.54	809	0.58	34.12	1.98	8.51
1TRB600	3.7	739	1.14	741	8.95	929	0.94	922	1.11	37.81	1.99	1.94

 $l_{
m yp}$  is the length of the yield plateau in  $arepsilon_{
m sy}.$ 

8 — Hanbo Zhu et al. DE GRUYTER

## 4 Parameter fitting of constitutive model for reinforcing steel

The constitutive model of reinforcing steel includes skeleton curves, hysteresis effects, buckling effects, and fatigue effects. Depending on the complexity of the model, indirect or direct methods can be adopted to fit the model parameters based on the experimental data of steel bars as follows.

### 4.1 Using the indirect method for parameter fitting

According to the brief functional relationship between the loading process and the material indicators in the model, the process of fitting model parameters using multi parameter nonlinear least squares (nonlinear least squares method) [35–37] is called the indirect method. Based on Eqs. (1)–(4) of the functions and tensile test data, the skeleton curve parameters of Steel01, Steel02, Steel4, Reinforcing Steel, Ramberg–OsgoodSteel, and SteelMPF models for HRB400 and HTRB600 steel bars are calculated, as listed in Table 2. The monotonic loading skeleton curve parameters including yield points ( $\varepsilon_{\rm sy}$ ,  $\sigma_{\rm sy}$ ), initial strengthening points ( $\varepsilon_{\rm si}$ ,  $\sigma_{\rm si}$ ), limit points ( $\varepsilon_{\rm sp}$ ,  $\sigma_{\rm sp}$ ), and damage points ( $\varepsilon_{\rm su}$ ,  $\sigma_{\rm su}$ ) are shown in Figure 8. In addition to the above eigenvalue parameters, parameters such as b,  $E_{\rm s}$ ,  $E_{\rm sh}$ , and strain ductility ratio  $l_{\rm vp}$  are also calculated in Table 3.

The Hysteretic and Pinching4 models are segmented linear models. Limiting the starting point position, the method of adaptive polyline fitting based on the least squares method is used to automatically find the segmentation point, fit the polyline skeleton curve, and find the coordinates of the polyline feature points in the model, as shown in Tables 4 and 5. Based on the skeleton curves determined by the above parameters, the indexes such as energy dissipation, maximum strain, maximum stress, and unloading stiffness in each loading cycle are calculated using the functional expressions of the Menegotto–Pinto dynamic hardening model, Stanton–Niven isotropic hardening model, and three-line damage hysteresis model. The main functions are expressed as Eqs. (5)–(15). Figure 9 shows the flowchart for calculating the model parameters using the indirect method.

The parameters of the HRB400 and HTRB600 reinforcement models for partial follow-hardening and isotropic hardening models for HRB400 and HTRB600 steel bars are listed in Table 6. The Pinching4 model does not consider the buckling and fatigue effects, the hysteresis effect is expressed by the ductility, stiffness, and strength cumulative damage effect functions [35]. The meaning of the relevant parameters can be found in Pinching4 model [36]. The initial trilinear hysteresis curves of HRB400 and HTRB600 steel bars with ductility degradation, strength degradation, and stiffness degradation parameters are listed in Tables 7–9. Hysteretic model [37] also does not consider the buckling effect and fatigue effect, the hysteretic effect is expressed by the ductility, energy consumption cumulative damage effect function. The cyclic damage parameters of HRB400 and HTRB600 steel bars are listed in Table 10.

### 4.2 Using the direct method for parameter fitting

The direct method is mostly used for the computational process of fitting the parameters of material constitutive

Table 4: Hysteretic	material m	ndel skeleton	curve nara	meters
Table 4. Hysteretic	material ii	iodei skeietoii	curve para	meters

Steel bars	$\varepsilon_{\rm H1}~(10^{-3})$	σ <sub>H1</sub> (MPa)	$\varepsilon_{\rm H2}~(10^{-3})$	σ <sub>H2</sub> (MPa)	$\varepsilon_{\rm H3}~(10^{-3})$	σ <sub>H3</sub> (MPa)
HRB400	2.40	472.98	1.505	652.63	1.546	516.25
HTRB600	3.40	751.51	0.802	958.15	1.638	789.14

Table 5: Pinching4 Material model skeleton curve parameters

Steel bar	$\delta_{P1}$ (10 $^{-3}$ )	$\sigma_{p1}$ (MPa)	$\delta_{P2}$ (10 $^{-2}$ )	σ <sub>ρ2</sub> (MPa)	$\delta_{P3}$ (10 $^{-1}$ )	σ <sub>ρ3</sub> (MPa)	$\delta_{P4} \ (10^{-1})$	σ <sub>p4</sub> (MPa)
HRB400	2.20	432.46	6.94	590.90	1.545	619.46	1.546	516.25
HTRB600	3.30	722.98	4.40	891.77	0.901	935.64	1.638	789.14

Note:  $(\delta_{Pb} \ \sigma_{pi})$ , i = 1, 2, 3, 4 denotes the four strain-stress characteristic points of the Pinching4 model skeleton curve.

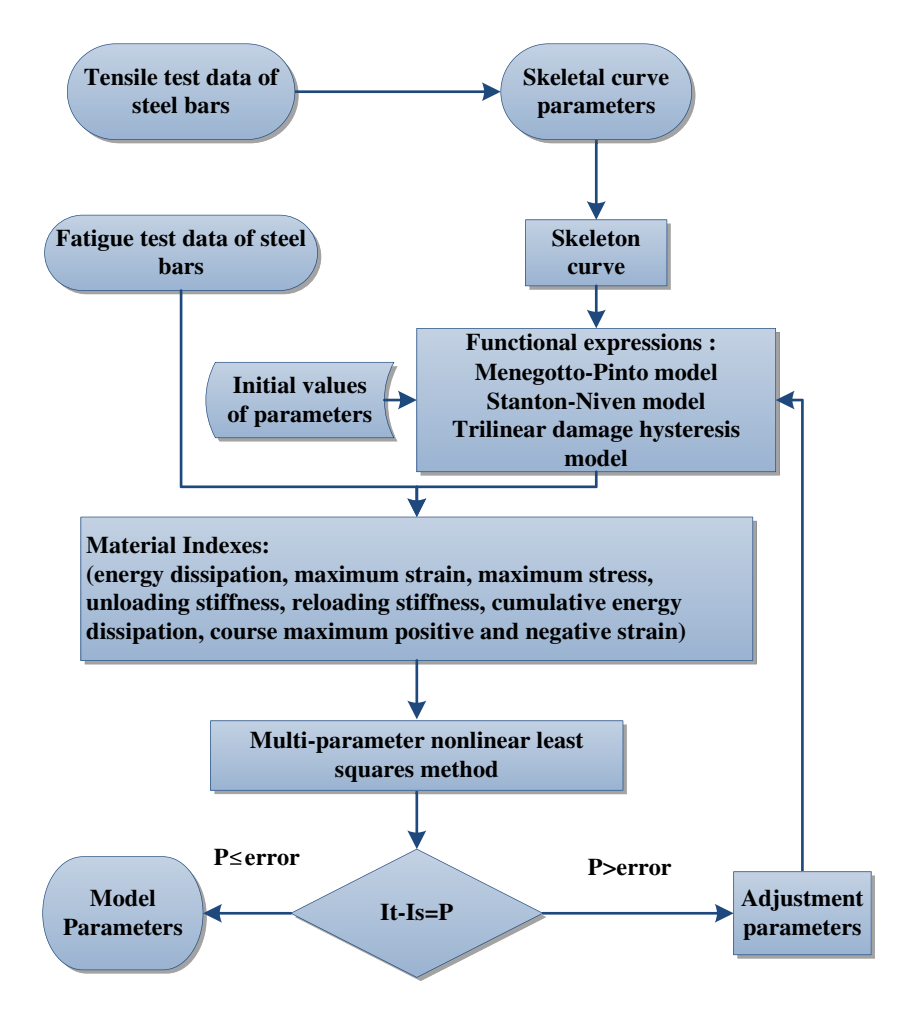


Figure 9: Flowchart for calculating the model parameters using the indirect method.

models with complex functional forms. The parameters of Coffin–Manson fatigue model and Adam Zsarnóczay isotropic hardening model are calculated using this method, as shown in Table 11. Figure 10 shows the flowchart for calculating the model parameters using the direct method.

Through trial calculations, it has been proven that when fitting a multi-parameter nonlinear univariate function, the maximum variation in the difference gradient is 0.1, the minimum variation is  $10^{-4}$ , the iteration increment step is 100 steps, the lower bound of the iterative

convergence tolerance step is  $10^{-6}$ , and the lower bound of the objective function variation is  $10^{-6}$ , the convergence stability is the highest, and the operation speed is the fastest. The Adam Zsarnóczay model simulates the isotropic strengthening effect by dividing three linear asymptotes and defining the cumulative function of plastic deformation. In Table 11, for the Adam Zsarnóczay model, the parameter fitting results for the initial strengthening ratio  $b_i$  and the saturation strengthening ratio  $b_l$  have the worst convergence. The main reason is that the monotonic

Table 6: Reinforcement hardening model parameters

Steel bar			Menegotto-l	Pinto model				Stanton-I	Niven Model	
	R <sub>0</sub>	A <sub>1</sub>	A <sub>2</sub>	R <sub>1</sub>	R <sub>2</sub>	R <sub>3</sub>	<i>a</i> <sub>1</sub>	<b>a</b> <sub>2</sub>	<b>a</b> <sub>3</sub>	a <sub>4</sub>
HRB400	35.2	0.966	0.213	0.323	18.1	10.39	0.0089	1.012	0.0089	1.012
HTRB600	43.1	0.954	0.0343	0.355	18.0	4.16	0.0185	0.993	0.0185	0.993

Note: The expressions of the parameters of the Menegotto–Pinto model in the Reinforcing Steel model are different from the other models;  $a_1$ ,  $a_2$ ,  $a_3$ , and  $a_4$  are all isotropic hardening parameters.

**Table 7:** Parameters of the trilinear hysteresis curve ductile degradation damage model

Steel bar	a <sub>d</sub> (10 <sup>-1</sup> )	b <sub>d</sub> (10 <sup>-2</sup> )	c <sub>d</sub> (10 <sup>-1</sup> )	d <sub>d</sub> (10 <sup>-3</sup> )	D <sub>dlim</sub> (10 <sup>-2</sup> )
HRB400	-2.352	9.91	2.003	-6.264	3.139
HTRB600	-1.591	14.65	1.310	18.70	5.757

Note:  $a_d$ ,  $b_d$ ,  $c_d$ ,  $d_d$ , and  $D_{dlim}$  are all floating-point values controlling cyclic degradation model for reloading stiffness degradation.

**Table 8:** Parameters of the trilinear hysteresis curve strength degradation damage model

Steel bar	a <sub>f</sub> (10 <sup>-1</sup> )	<i>b</i> <sub>f</sub> (10 <sup>-1</sup> )	c <sub>f</sub> (10 <sup>-3</sup> )	d <sub>f</sub> (10 <sup>-1</sup> )	D <sub>flim</sub> (10 <sup>-1</sup> )
HRB400	9.553	-3.419	5.124	-12.25	1.038
HTRB600	3.430	-2.665	6.652	-8.010	1.023

Note:  $a_f$ ,  $b_f$ ,  $c_f$ ,  $d_f$ , and  $D_{flim}$  are all floating-point values controlling cyclic degradation model for strength degradation.

**Table 9:** Parameters of the trilinear hysteresis curve stiffness degradation damage model

Steel bar	a <sub>k</sub> (10 <sup>-1</sup> )	b <sub>k</sub> (10 <sup>-1</sup> )	c <sub>k</sub> (10 <sup>-3</sup> )	d <sub>k</sub> (10 <sup>-1</sup> )	D <sub>klim</sub> (10 <sup>-1</sup> )
HRB400	-29.82	32.95	22.55	3.392	2.167
HTRB600	0.660	3.626	9.574	18.24	3.935

Note:  $a_k$ ,  $b_k$ ,  $c_k$ ,  $d_k$ , and  $D_{klim}$  are all floating-point values controlling cyclic degradation model for unloading stiffness degradation.

Table 10: Hysteretic model rebar cyclic damage parameters

Steel bar	$P_x$ (10 <sup>-1</sup> )	$P_y$ (10 <sup>-1</sup> )	D <sub>1</sub> (10 <sup>-3</sup> )	$D_2 (10^{-1})$	β (10 <sup>-1</sup> )	
HRB400	-29.82	32.95	22.55	3.392	2.167	
HTRB600	0.660	3.626	9.574	18.24	3.935	

Note:  $P_x$  = pinching factor for strain during reloading,  $P_y$  = pinching factor for stress during reloading,  $D_1$  is the damage caused by ductility,  $D_2$  is the damage caused by energy,  $\beta$  is the power used to determine the degraded unloading stiffness based on ductility.

loading ultimate strains  $\varepsilon_{su}$  of HRB400 and HTRB600 steel bars are  $67\varepsilon_{sy}$  and  $25\varepsilon_{sy}$ , respectively, much larger than the amplitude of reciprocal loading conditions in the fatigue tests (1–2 times  $\delta_y$ ) [38], which cannot reflect the isotropic strengthening effect of large deformation reciprocal loading. Therefore, the parameters can meet the accuracy requirements of the small-amplitude reciprocal loading simulation when they are taken within the given interval.

Constitutive model parameters for other types of steel bars can also be determined based on the corresponding tensile and fatigue tests of the bars. If the test data are insufficient, the linear difference between the parameters of HRB400 and HTRB600 steel bars can be approximated based on the yield strength of reinforcing steel. Based on tensile and fatigue test data of HRB400 and HTRB600 steel bars, the parameters in nine common reinforcement principal structure models are fitted in OpenSees software, laying the foundation for the selection of constitutive models for reinforcing steel.

### 5 Analysis and discussion of simulation results

### 5.1 Simulation of monotonic tensile test

In Table 2, among the nine constitutive models for reinforcing steel, the Dodd–Restrepo Steel model and Ramberg–Osgood Steel model cannot represent the material damage accumulation phenomenon under constant amplitude loading, while the SteelMPF model is an asymmetric model based on the Steel02 model, thus the Dodd–Restrepo Steel, Ramberg–Osgood Steel, and SteelMPF models are excluded. Based on the tensile and fatigue test data of HRB400 and HTRB600 steel bars, the fitting effects of Steel01 model, Steel02 model, Steel4 model, Reinforcing Steel model, Pinching4 model, and Hysteretic model are

Table 11: Skeleton, hysteresis, and fatigue model parameters for reinforcing steel

Steel bars					Adam Zs	arnóczay mode	el .			
	Coffin-Ma	anson fatigue ı	model		Chang-	Mander model			Chang–M	ander model
	C <sub>f</sub>	C <sub>d</sub>	Α	b <sub>i</sub>	ρί	b <sub>I</sub>	Ri	l <sub>yp</sub>	a <sub>c1</sub>	I <sub>i</sub>
HRB400 HTRB600	0.224 0.231	0.322 0.290	0.377 0.394	$10^{-5} \sim 10^{-10}$ $10^{-5} \sim 10^{-10}$	1.01 1.05	$10^{-5} \sim 10^{-10}$ $10^{-5} \sim 10^{-10}$	10 15	8.51 1.94	6.36 11.80	0.01 0.01

Note:  $b_i$  is the initial hardening ratio;  $b_l$  is the saturated hardening ratio;  $\rho_i$  specifies the position of the intersection point between initial and saturated hardening asymptotes;  $R_i$  controls the exponential transition from initial to saturated asymptote;  $I_{yp}$  is the length of the yield plateau in  $\varepsilon_{sy}$ ;  $a_{c1}$  is the hardening constant;  $I_i$  is the isotropic hardening limit.

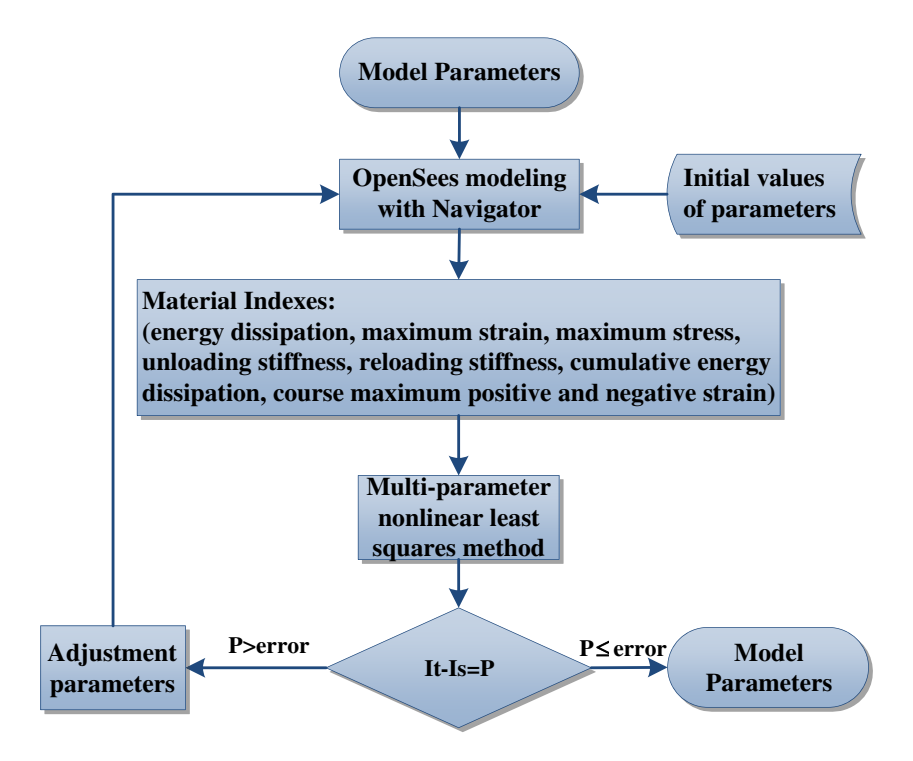


Figure 10: Parameter fitting process based on direct method.

compared, from which the constitutive model with the highest simulation accuracy is found. The tensile property of HRB400 and HTRB600 steel bars are simulated, which are compared with the tensile test results in Figure 11.

The stresses in elastic and platform sections of Pinching4 and Hysteretic models are much higher than the experimental values. The simulation accuracy of the multi-section model is ranked as follows: Pinching4 model > Hysteretic model > Steel01 model, with the priority of

ensuring the overall alignment uniformity. Although the finite multi-section line simulates the stress-strain curve of steel bars with poor overall performance, increasing the number of segments can improve the simulation accuracy. The Steel02 model has nonlinear excess at the segments, which is accurately simulated in elastic and platform segments. However, the strengthening and damage segments are characterized by linear segments, and the fitting accuracy is obviously insufficient. In contrast, the Steel4 model and Reinforcing Steel model have higher

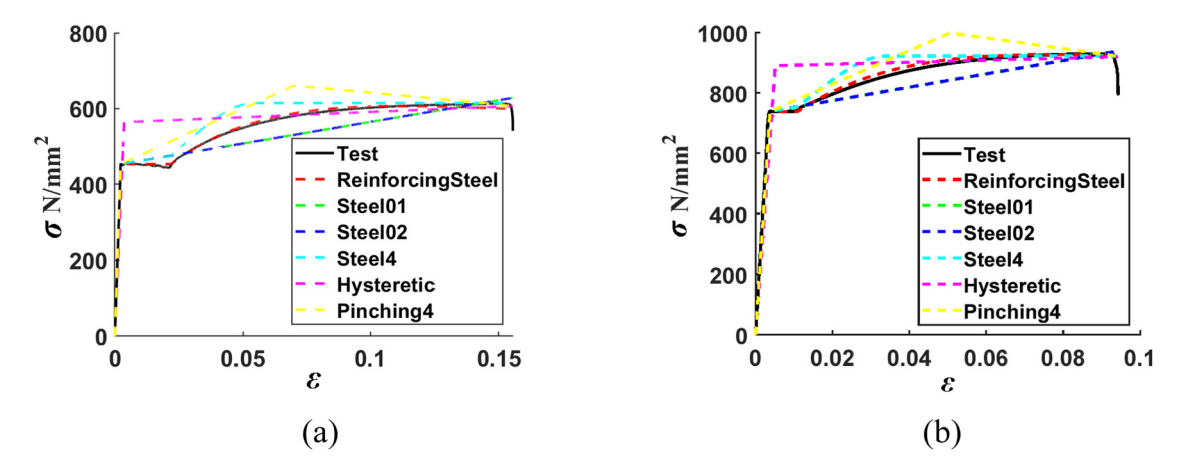


Figure 11: Comparison of simulation results and tensile test results. (a) HRB400 steel bars. (b) HTRB600 steel bars.

fitting accuracy throughout the monotonic loading process. Among them, the Reinforcing Steel model is described by continuous curves in the strengthening and descent sections, and the fitting results are closer to the actual results.

### 5.2 Simulation of fatigue test

The fatigue properties of HRB400 and HTRB600 steel bars are simulated. The simulation results of HRB400 steel bars with 1% strain amplitude and HTRB600 with 2% strain amplitude were selected for comparison with the low-cycle fatigue test results. To better compare the strain–stress relationship throughout the entire loading process, the cumulative strain  $\varepsilon_{\rm AC}$  is the independent variable and the cumulative strain–stress relationship is established. The half-cycle process of loading and unloading at different segmentation points is intercepted for comparison.

The simulated and experimental stress–strain curves for HRB400 steel bars with 1% strain amplitude are compared in Figure 12. In Figure 12,  $\varepsilon$  is the strain of the steel bar. The strain in steel bar is usually measured using an extensometer. An extensometer is a mechanical device that accurately measures the strain in a material. It usually consists of two movable arms that can be placed at either end of the steel bar at the location where it is being measured. As the steel bar is strained, the arms of the extensometer

move with it, and by measuring the relative distances of the extensometer arms, the displacement deformation of the steel bar over a standard test length is calculated, and ultimately converted to strain.

The Steel01 model and Pinching4 model cannot reflect the pinching effect of the steel bar, and the Pinching4 model has relatively higher calculation accuracy. When the Hysteretic model is applied to simulate the hysteresis curve after yielding, the simulated maximum stress is 20% higher than that obtained from the test, and the simulated pinching effect is too large. The linear segmentation model is faster in calculation and can roughly reflect the damage accumulation process of reinforcement steel, but it cannot consider the characteristics of strength, stiffness, and pinching effect due to the limited characteristic points of skeleton curve and hysteretic curve addition and removal. The above conclusions are determined by the characteristics of the linear segmentation model and are almost unrelated to the parameter values. The cumulative strain of HRB400 steel bars under 1% strain amplitude loading condition ranges from 0 to 13.42.

The simulated and experimental stress accumulated change with the strain of HRB400 steel bars at 1% strain amplitude loading.

There is a law that under fatigue loading conditions, the bearing capacity keeps decreasing, but the rate of decline slows down. The Hysteretic, Pinching4, Steel01, and Steel02 models cannot simulate the stress degradation process under fatigue loading, while the Steel4 model can simulate the stress process of the bearing capacity, but the

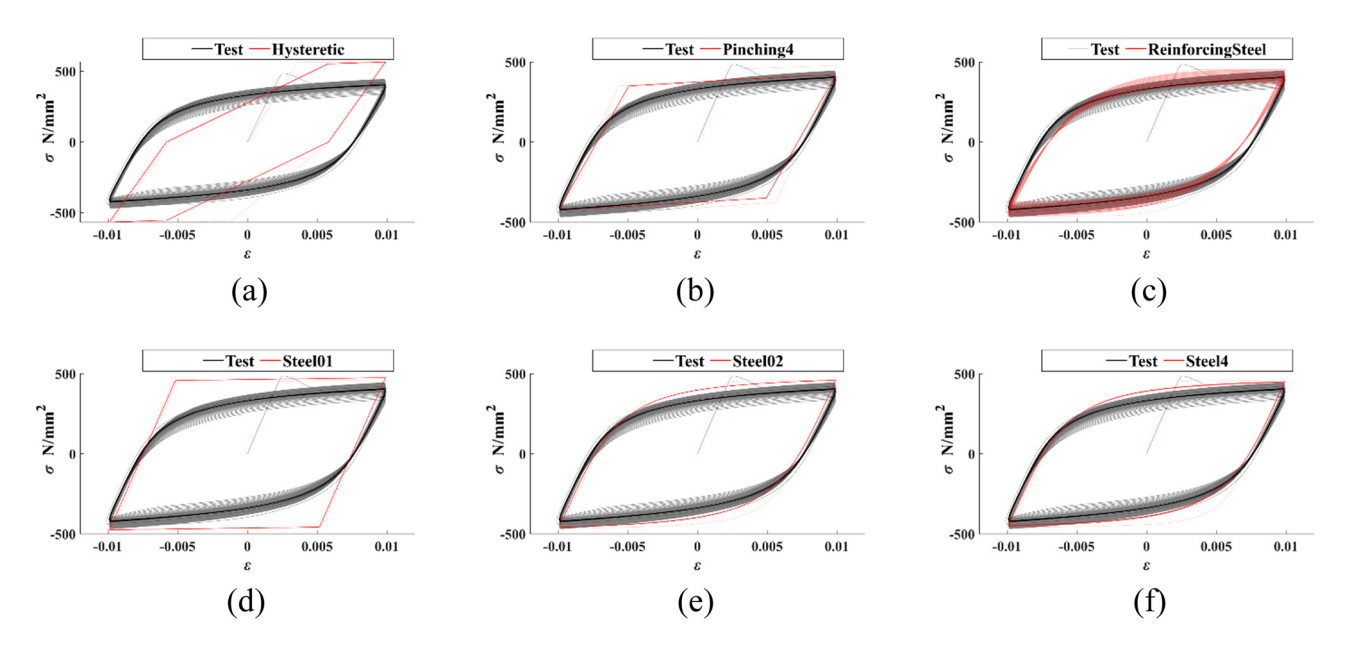
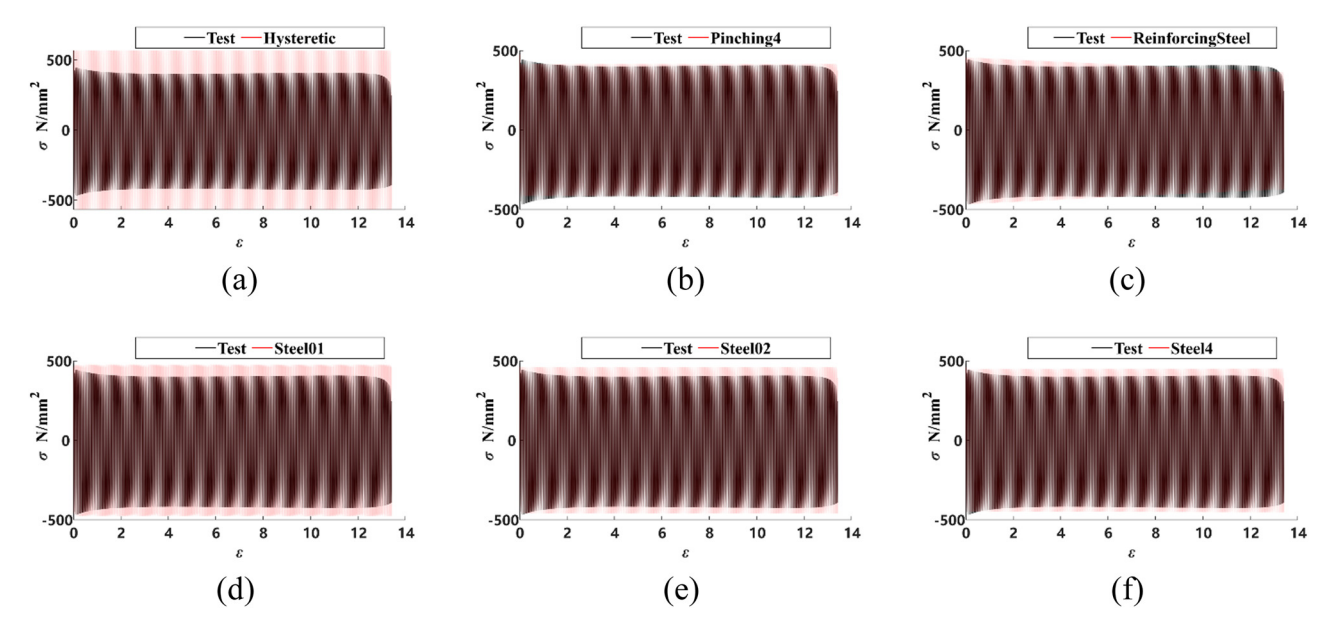


Figure 12: The experimental and simulated stress-strain curves for HRB400 steel bars under 1% strain amplitude. (a) Hysteretic model. (b) Pinching4 model. (c) Reinforcing Steel model. (d) Steel01 model. (e) Steel02 model. (f) Steel4 model.



**Figure 13:** The simulated and experimental stress accumulated change with the strain of HRB400 steel bars under 1% strain amplitude loading. (a) Hysteretic model. (b) Pinching4 model. (c) Reinforcing Steel model. (d) Steel01 model. (e) Steel02 model. (f) Steel4 model.

stress shows an increasing trend, which is inconsistent with the actual situation. Only Reinforcing Steel model can better reflect the continuous degradation trend of the reinforcing steel stress (Figure 13).

On this basis, the experimental results of the half-cycle loading and unloading processes at different segmentation points with the simulation results using different models are further compared, as shown in Figure 14. At different

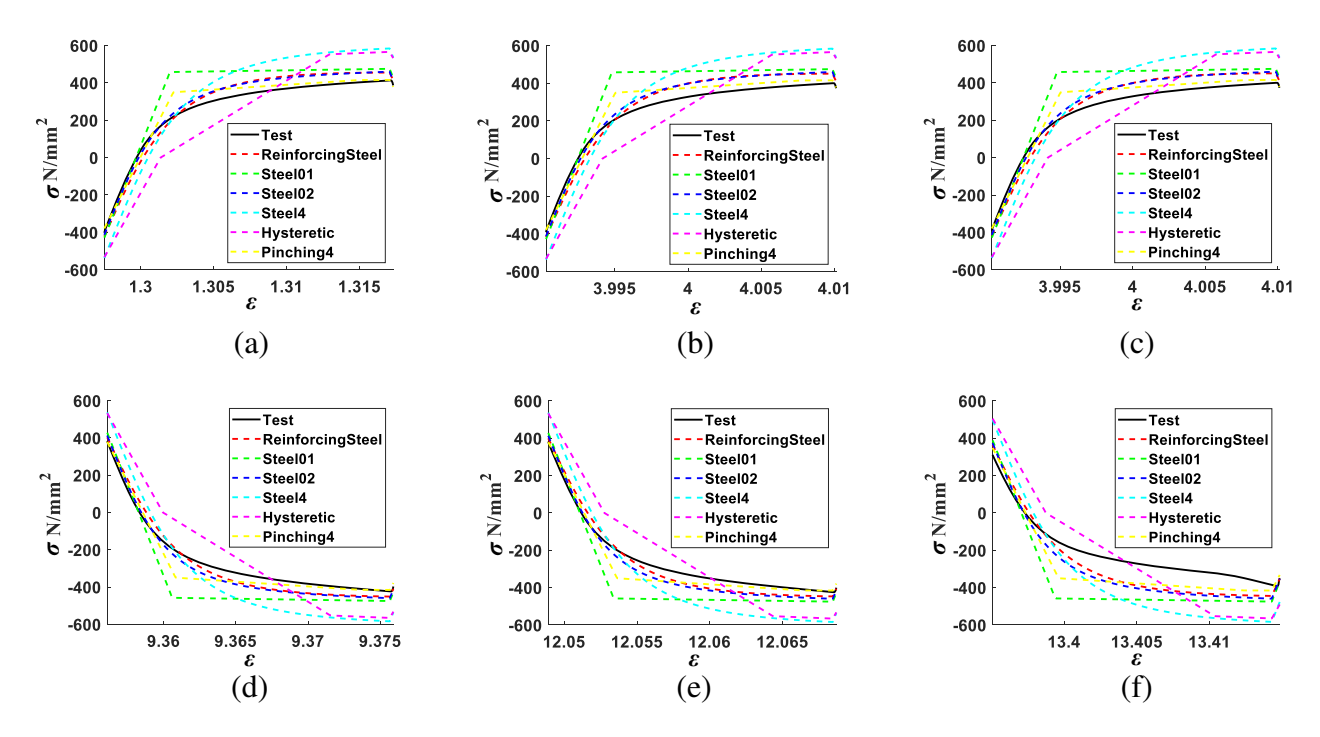


**Figure 14:** Comparison of the experimental results of the half-cycle loading and unloading processes at different segmentation points with the simulation results using different models. (a) 1.2975–1.3173. (b) 3.9903–4.0101. (c) 6.6831–6.7029. (d) 9.3561–9.3759. (e) 12.0489–12.0687. (f) 13.3951–13.4148.

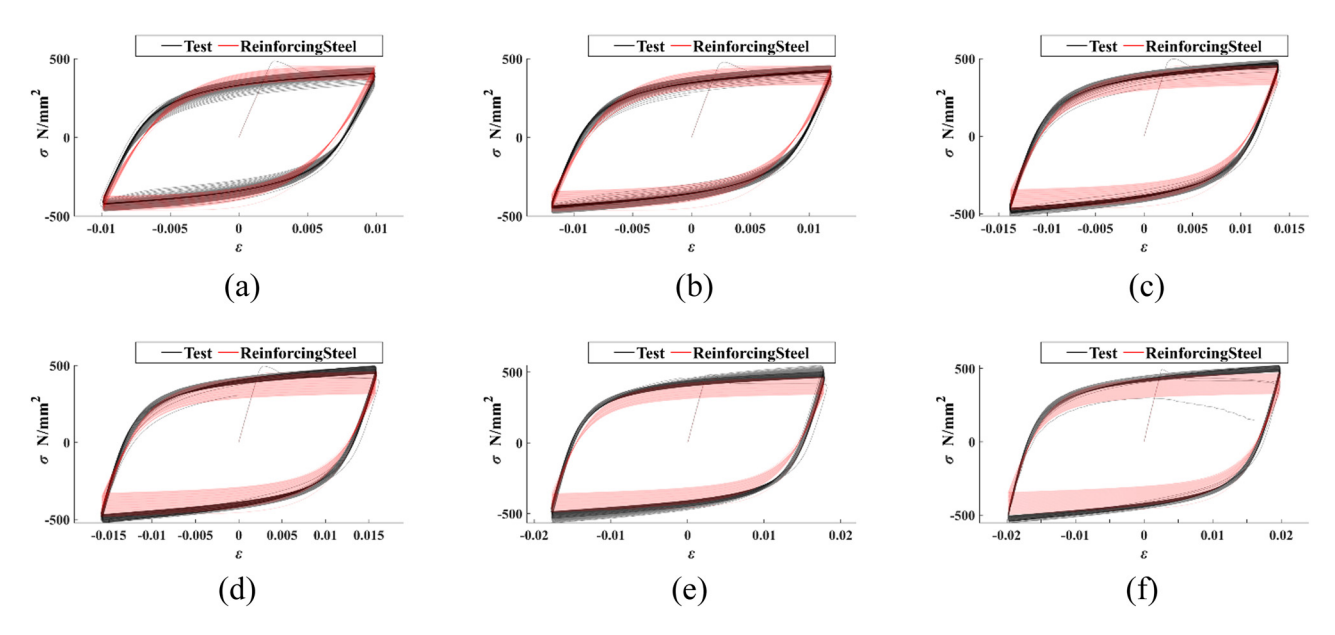


**Figure 15:** Comparison of fatigue test values of HRB400 steel bars with simulated values using Reinforcing Steel model. (a) 1% strain amplitude. (b) 1.2% strain amplitude. (c) 1.4% strain amplitude. (d) 1.6% strain amplitude. (e) 1.8% strain amplitude. (f) 2.0% strain amplitude.

stages of loading the Hysteretic, Pinching4, and Steel01 models using polyline fitting cannot match the experimental curves, in which the pinching of the simulated materials using Steel01 and Pinching4 models is too small, while the pinching of the simulated materials of Hysteretic model is too large. The simulated curve using the Steel4 and Reinforcing Steel models are very close at the beginning of loading, and the stress in the test gradually decreased with loading, and the pinching phenomenon gradually becomes

significant. The simulation accuracy of the Steel02 and Steel4 models gradually becomes worse, and only Reinforcing Steel model maintained the simulation accuracy. The simulation results for HRB400 and HTRB600 steel bars under different constant strain amplitudes show similar patterns.

Figure 15 shows the comparison of fatigue test values of HRB400 steel bars with simulated values using Reinforcing Steel model. Figure 16 shows the comparison of fatigue test values of HRB400 steel bars with simulated values

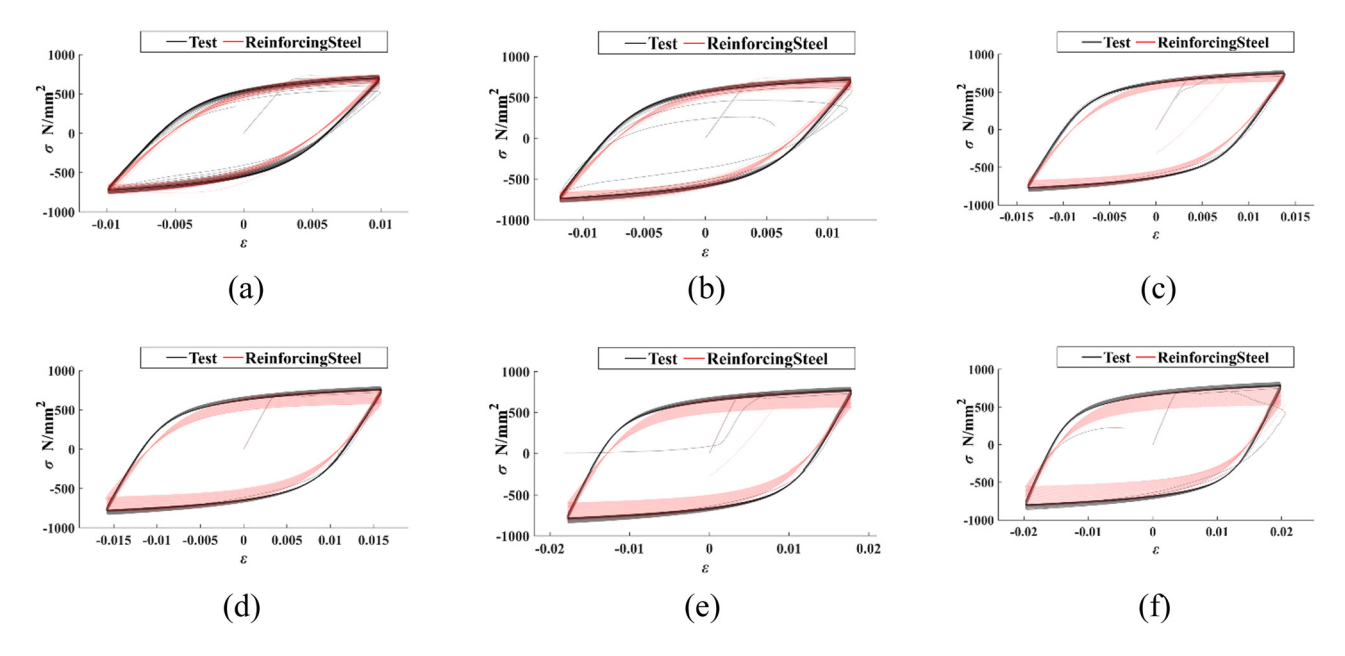


**Figure 16:** Comparison of fatigue test values of HTRB600 steel bars with simulated values using Reinforcing Steel model. (a) 1% strain amplitude. (b) 1.2% strain amplitude. (c) 1.4% strain amplitude. (d) 1.6% strain amplitude. (e) 1.8% strain amplitude. (f) 2.0% strain amplitude.

using Reinforcing Steel model. Reinforcing Steel, Steel02, and Steel4 models are nonlinear segmented models. They have higher simulation accuracy than linear segmented models and can better simulate the pinching effect of the envelope, strength, and degradation characteristics of the stiffness during reciprocal loading. The Steel02 model cannot simulate the degradation characteristics of the stiffness, strength, and energy dissipation capacity under fatigue loading, while Steel4 and Reinforcing Steel models consider the fatigue effect of the material using the strength discount function and Coffin–Manson fatigue model, respectively.

In summary, among the three linear segmentation models, the Pinching4 model has the largest number of linear segments, which ensures the simulation accuracy of the skeleton curve while considering the effects of maximum deformation amplitude and cumulative energy dissipation on material ductility, strength, and stiffness of loading and unloading. Among the nonlinear segmentation models, Reinforcing Steel and Steel4 models have the highest simulation accuracy, but the former can consider the buckling effect of longitudinal reinforcement due to insufficient stirrups, so the Reinforcing Steel model is chosen to simulate the constitutive relationship of reinforcement steel. The constitutive model parameters are determined using the indirect and direct methods for finite element simulation of reinforced concrete columns.

### 5.3 Seismic performance indexes

The hysteresis curve reflects the energy dissipation capacity, deformation characteristics, and stiffness and strength degradation of the member under fatigue loading, which can be quantitatively analyzed by the cumulative hysteresis dissipation coefficient, equivalent viscous damping coefficient, residual deformation, strength and stiffness degradation ratio, and other indicators. The specified cumulative hysteresis dissipation coefficient  $E_{N,m}$  and the equivalent viscous damping coefficient  $\xi_{\rm eq}$  are two important energy dissipation indexes, as shown in Eqs. (16) and (17).

$$E_{\mathrm{N},m} = \frac{1}{\sigma_{\mathrm{sy}} \varepsilon_{\mathrm{sy}}} \sum_{i=1}^{m} S_i, \tag{16}$$

$$\xi_{\text{eq},i} = \frac{S_i}{2\pi (S_{\Delta \text{OAB}} + S_{\Delta \text{OCD}})},\tag{17}$$

where  $E_{{
m N},m}$  is the cumulative hysteresis dissipation coefficient of the member after m loading cycles,  $S_i$  is the area enclosed by the ith hysteresis loop, and  $S_{\Delta {
m OAB}}$  and  $S_{\Delta {
m OCD}}$  are the areas of the two triangles OAB and OCD (Figure 17).  $\xi_{{
m eq},i}$  is the equivalent viscous damping coefficient for the ith loading cycle.

Strength and stiffness degradation refers to the process that the bearing capacity under the same amplitude and stiffness under different amplitudes continue to decrease with the increase in the loading cycle after cyclic loading of the member, which can be calculated by strength degradation coefficient  $\lambda$  and loop stiffness K, respectively, see Eqs. (18) and (19).

$$\lambda_j^i = \frac{\sigma_j^i}{\sigma_i^i},\tag{18}$$

$$E_j^i = \frac{\sum_{i=1}^{i=n} \sigma_j^i}{\sum_{i=1}^{i=n} \varepsilon_i^i},\tag{19}$$

where  $\sigma^i_j$ ,  $\varepsilon^i_j$ ,  $\lambda^i_j$  and  $E^i_j$  are the load maximum, displacement amplitude, strength degradation factor, and loop stiffness at the *i*th cycle of the *j*th level of displacement amplitude, respectively.

Taking the steel bar 1.0 and 1.8% specimens with 1.0 and 1.8% strain amplitudes as examples, the three indicator indexes,  $\xi_{eq}$ ,  $\lambda$ , and K, and the experimental and simulation results of HRB400 and HTRB600 steel bars under different strain amplitudes are compared and analyzed. Figure 18 shows the change curves of seismic indexes of HRB400 steel bars with the increase in loading cycles. Figure 19 shows the change curves of seismic indexes of HTRB600 steel bars with the increase in loading cycles. The equivalent viscous damping coefficient  $\xi_{eq}$  drops abruptly with the increase in the loading cycle, then decreases smoothly and slowly, and the member fails when it decreases to 0.7-0.9. Reinforcing Steel and Steel02 models simulate  $\xi_{\rm eq}$  better, among which Reinforcing Steel model simulates the process of first a sharp drop and then a smooth drop, but neither can simulate the sudden drop damage process after the smooth section. Starting from the second cycle,  $\lambda$  rises from 0.85 to 0.9 with the decrease in the

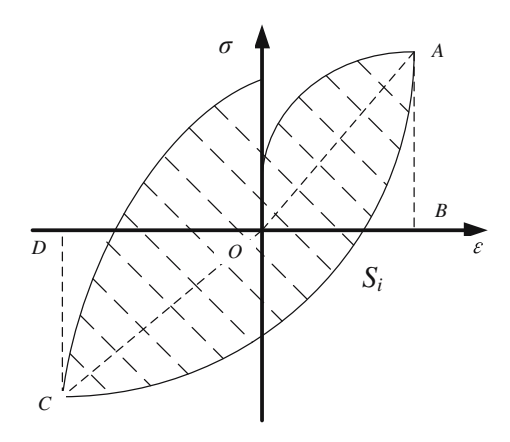
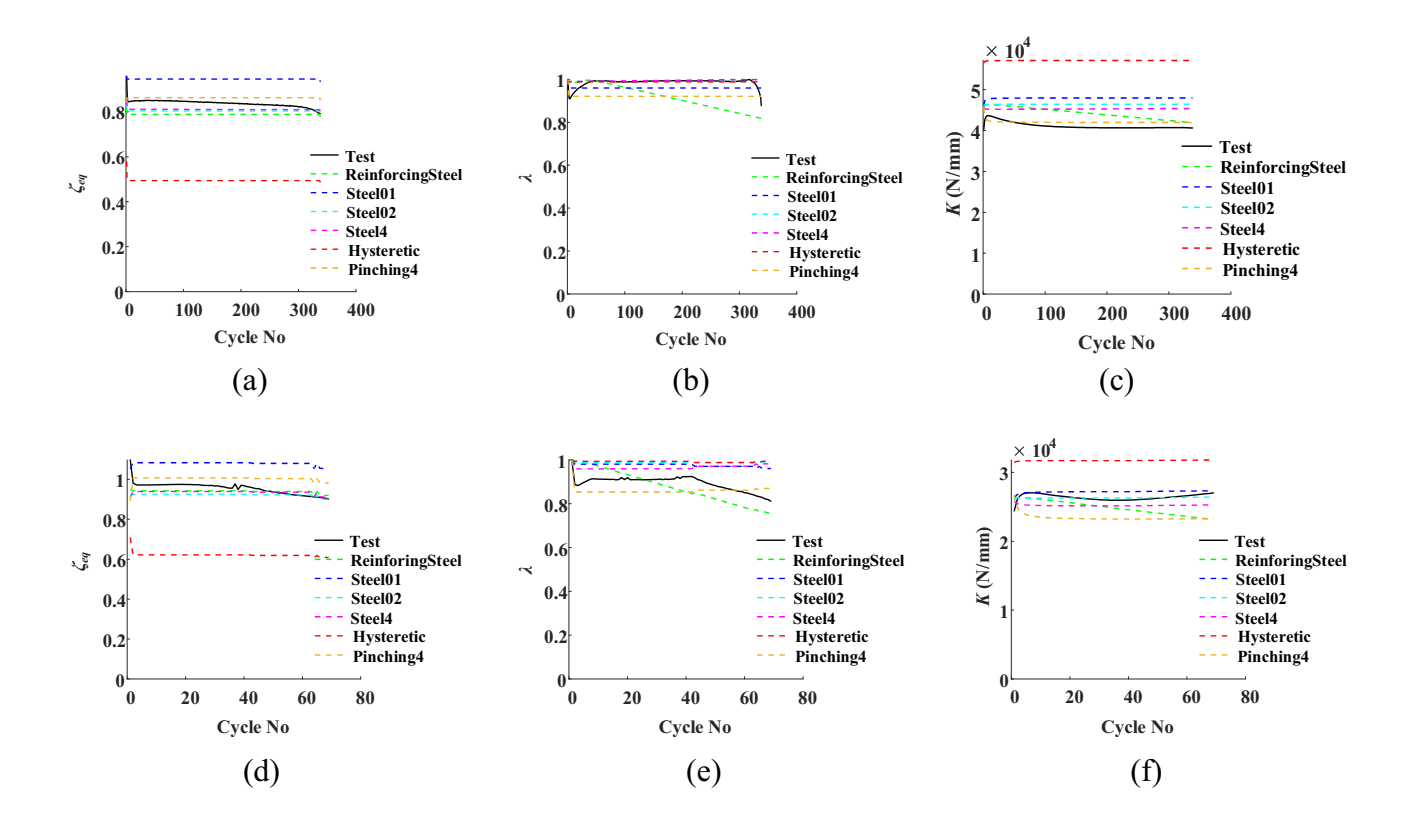
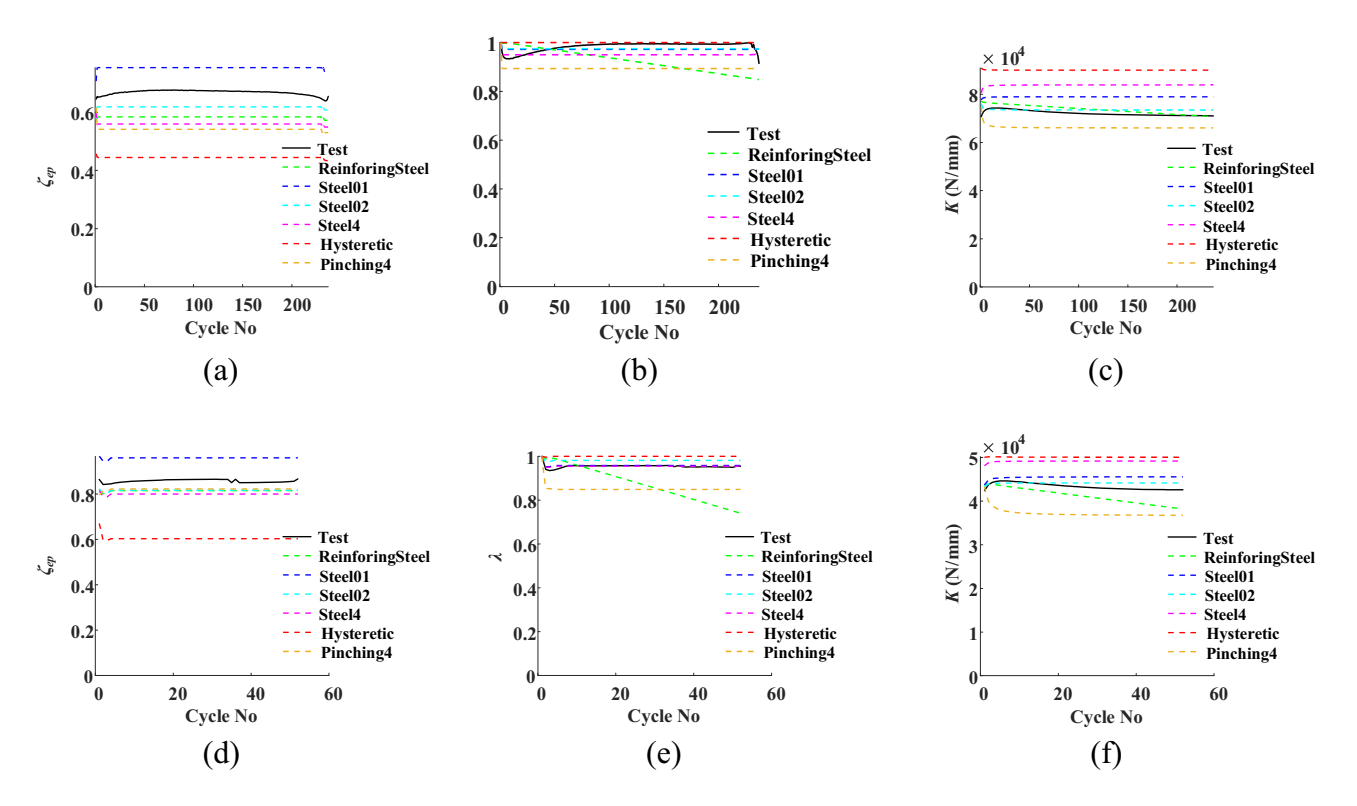


Figure 17: Hysteresis loop schematic.



**Figure 18:** The change curves of seismic indexes of HRB400 steel bars with the increase in the laoding cycle. (a)  $\xi_{eq}$  – 1.0%. (b)  $\lambda$  – 1.0%. (c) K – 1.0%. (d)  $\xi_{eq}$  – 1.8%. (e)  $\lambda$  – 1.8%. (f) K – 1.8%.



**Figure 19:** The change curves of seismic indexes of HTRB600 steel bars with the increase in the loading cycle. (a)  $\xi_{\rm eq}$  – 1.0%. (b)  $\lambda$  – 1.0%. (c) K – 1.0%. (d)  $\xi_{\rm eq}$  – 1.8%. (e)  $\lambda$  – 1.8%. (f) K – 1.8%.

**Table 12:** Similarity of seismic performance indexes for HRB400 steel bars under 1.4% strain amplitude

Model	R <sub>Fp</sub>	R <sub>EN,m</sub>	$C_{ m \xi eq}$	$c_{\lambda}$	C <sub>K</sub>	Mean value
Reinforcing Steel	0.94	1.00	0.67	0.45	0.86	0.76
Steel01	0.98	0.69	0.34	0.31	0.62	0.59
Steel02	0.95	0.83	0.39	0.34	0.63	0.63
Steel4	0.94	0.70	0.89	0.52	0.68	0.69
Hysteretic	0.87	0.72	0.34	0.31	0.62	0.57
Pinching4	0.96	0.41	0.58	0.48	0.62	0.61

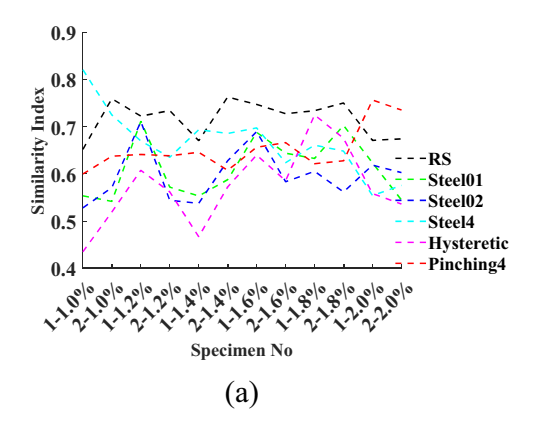
loading cycle, it enters the plateau stage when it rises to 0.9-0.98, and then it continues to fall slowly or abruptly causing damage to the member. The value of  $\lambda$  at 1.0% strain amplitude loading is higher than the value of  $\lambda$ under 1.8% strain amplitude loading. Throughout the loading process, the Steel02 model simulates  $\lambda$  with high accuracy, and only the Reinforcing Steel model can simulate the falling section of the member after the platform section. However, none of the models could make an accurate simulation of  $\lambda$ . K experienced a short rise with the increase in the loading cycle, followed by a deceleration and decline to smooth out, and finally a sudden drop to damage. Compared with the other models, the Reinforcing Steel and Steel02 models simulate K more accurately, but the simulation accuracy for the falling section is lower, where Steel02 model underestimates the falling trend of K, while Reinforcing Steel overestimates the falling trend of K. It can be concluded that the Reinforcing Steel model simulates the cyclic characteristic indexes best.

In order to analyze the simulation accuracy of bearing capacity,  $R_{\rm f}$  is used to represent the ratio of the minimum and maximum values of peak bearing capacity  $F_{\rm p}$  during cyclic loading.  $R_{\rm f,s}$  is used to represent the simulated value of  $R_{\rm f}$ ,  $R_{\rm f,t}$  is used to represent the test value of  $R_{\rm f}$  let  $R_{\rm Fp}$  =

 $R_{\rm f,s}/R_{\rm f,t}$ . In order to analyze the simulation accuracy of energy dissipation,  $R_{\rm E}$  is used to represent the ratio of the minimum and maximum values of cumulative hysteresis energy dissipation coefficient  $E_{N,m}$ .  $R_{E,s}$  is used to represent the simulated value of  $R_{\rm E}$ ,  $R_{\rm f,t}$  is used to represent the test value of  $R_{\rm E}$ , let  $R_{\rm EN,m} = R_{\rm E,s}/R_{\rm E,t}$ . According to the hysteresis curves, the change curves of  $\xi_{eq}$ ,  $\lambda$ , and K with the increase in loading cycles are obtained. To compare the correlation between the simulated and experimental curves, the Pearson correlation coefficient [39], the distance correlation coefficient [40], and the maximum information coefficient algorithm [41] are applied to calculate the correlation coefficients of  $\xi_{eq}$ ,  $\lambda$ , and K curves, which are denoted as  $C_{\xi_{eq}}$ ,  $C_{\lambda}$ , and  $C_K$ , respectively. Table 12 gives the similarity of seismic performance indexes of the experimental and simulated results for HRB400 steel bars under 1.4% strain amplitude. The mean values of the five similarity parameters are used to describe the simulation accuracy of HRB400 steel bars under 1.4% strain amplitude, with Reinforcing Steel model fitting the highest accuracy.

Similarly, the simulation accuracy can be obtained for HRB400 and HTRB600 steel bars under different strain amplitudes, as shown in Figure 20(a) and (b). Comparing the similarity between the simulation and test results under the two sets of constant strain amplitude loading conditions, it can be seen that the simulation accuracy of Reinforcing Steel and Pinching4 models is higher for HRB400 steel bars. The simulation accuracy of Reinforcing Steel and Steel4 models is higher for HTRB600 steel bars. The Reinforcing Steel model has the highest simulation accuracy, but it decreases slightly with the change in strain amplitudes.

The similarity indexes of the experimental results and the simulation results of the Reinforcing Steel model for HRB400 and HTRB600 steel bars are obtained in Figure 21. The similarity of the Reinforcing Steel model for HRB400 steel bars is more than 65%, and the mean value of its



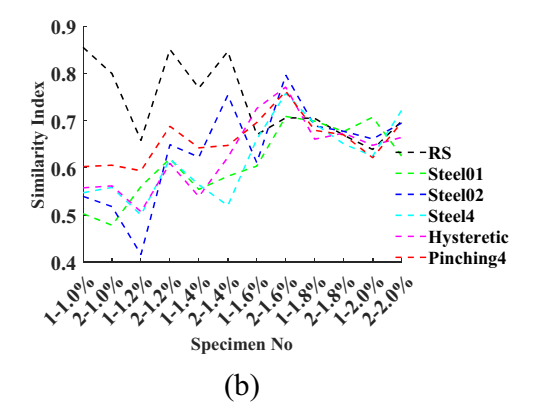
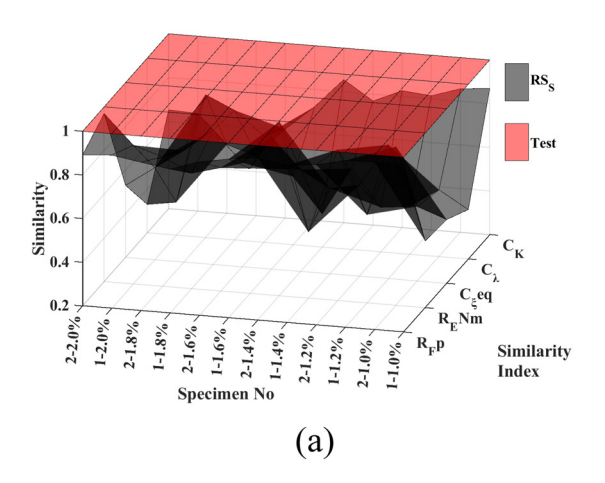


Figure 20: Similarity indexes of experimental and simulation results. (a) HRB400 steel bars. (b) HTRB600 steel bars.



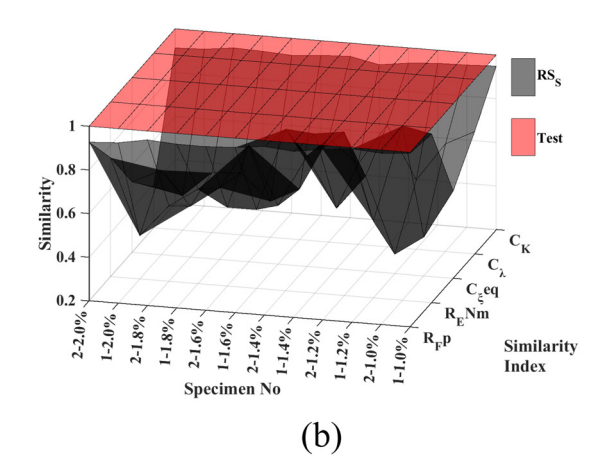


Figure 21: Similarity indexes of the experimental and the simulation results of the Reinforcing Steel model. (a) HRB400 steel bars. (b) HTRB600 steel bars.

similarity is 73%, while the mean value of the similarity of the other models does not exceed 65%. The similarity of the Reinforcing Steel model for HTRB600 steel bars is slightly lower than that for HRB400 steel bars, with the mean value of the similarity being 72%, and the mean value of the similarity for the other models also does not exceed 65%.

From the above analysis, it can be seen that the accuracy of fitting the parameters of the Reinforcing Steel model using direct and indirect methods is more than 72%. These two methods are the core of the automated determination of the material constitutive relationships and are in principle applicable to the determination of the constitutive model and multi-parameter calculations for any type of steel bars. For other types and strength grades of steel bars, the accuracy of modeling the material constitutive relationship needs to be further verified in subsequent studies.

### 6 Conclusion

In this article, the tensile and low-cycle fatigue properties of HRB400 and HTRB600 steel bars were first investigated experimentally. Then, the indirect and direct methods are proposed to fit the constitutive model parameters of reinforcing steel using OpenSees software. Finally, the simulation and experimental results, as well as the determination of the constitutive relationship of reinforcing steel are analyzed and discussed. The main conclusions are as follows:

 Based on the tensile and fatigue properties of HRB400 and HTRB600 steel bars, the hysteresis and fatigue parameters of Steel01, Steel02, Steel4, Hysteretic, and Reinforcing Steel models are calculated using direct and indirect multi-

- parameter nonlinear least squares methods, respectively. The direct and indirect methods proposed in this article can be used to establish the constitutive models of other types and strength grades of steel bars.
- 2) Based on the experimental results, an automated process of multi-parameter calculation of the constitutive model for reinforcing steel simulation accuracy evaluation of the constitutive model selection of the constitutive model is established based on the hybrid programming method of MATLAB and OpenSees software.
- 3) The simulation accuracy of the Reinforcing Steel model exceeds 72%, which is higher than that of the Steel01, Steel02, Steel4, Hysteretic and Pinching4 models.

Acknowledgments: The authors acknowledge Suqian University talent introduction scientific research startup fund project (School 2022XRC064), China; Suqian Sci &Tech (Grant No. K202342), China; the Natural Science Research Project of Jiangsu Province Colleges and Universities (21KJD560002), China; Suqian Natural Science Foundation Project (K202012), China; the research and innovation team of engineering structure seismic technology of Suqian University in 2020, China; Suqian City Guiding Science and Technology Plan Project (Z2020137), China; Research and Innovation Team Project of Suqian College (2021TD04), China; and the Fifth Provincial Research Funding Project of "333 Highlevel Talent Training" in 2020 (BRA2020241), China.

**Funding information:** This research has been supported by Suqian University talent introduction scientific research start-up fund project (School 2022XRC064), China; Suqian Sci &Tech (Grant No. K202342), China; the Natural Science Research

Project of Jiangsu Province Colleges and Universities (21KJD560002), China; Suqian Natural Science Foundation Project (K202012), China; the research and innovation team of engineering structure seismic technology of Suqian University in 2020, China; Suqian City Guiding Science and Technology Plan Project (Z2020137), China; Research and Innovation Team Project of Suqian College (2021TD04), China; and the Fifth Provincial Research Funding Project of "333 High-level Talent Training" in 2020 (BRA2020241), China.

**Author contributions:** All authors have accepted responsibility for the entire content of this manuscript and approved its submission.

Conflict of interest: The authors state no conflict of interest.

**Data availability statement:** The datasets generated and/ or analyzed during the current study are available from the corresponding author on reasonable request.

### References

- [1] National Standards of People's Republic of China. *Steel for the reinforcement of concrete: Part 1: Hot rolled plain bars: GB/T 1499.* 1-2017, Standards Press of China, Beijing, 2017 (in Chinese).
- [2] National Standards of People's Republic of China. Steel for the reinforcement of concrete: Part 2: ribbed bars: GB/T 1499. 2-2018, Standards Press of China, Beijing, 2018 (in Chinese).
- [3] Veprek, R. G., D. M. Parks, and A. S. Argon. Non-linear finite element constitutive modeling of mechanical properties of hard and superhard materials studied by indentation. *Materials Science and Engineering: A*, Vol. 422, No. 1–2, 2006, pp. 205–217.
- [4] Xiong, C., C. Zeng, and Y. Li. The constitutive relationship for corroded steel bars: Model and analysis. *Materials*, Vol. 12, No. 24, 2019, pp. 40–58.
- [5] Apostolopoulos, C. A. and V. Kappatos. Tensile properties of corroded embedded steel bars B500c in concrete. *International Journal of Structural Integrity*, Vol. 4, No. 2, 2013, pp. 275–294.
- [6] Zottis, J., Diehl C. A. T. S., Silva Rocha A. Evaluation of experimentally observed asymmetric distributions of hardness, strain and residual stress in cold drawn bars by FEM-simulation. *Journal of Materials Research and Technology*, Vol. 7, No. 4, 2018, pp. 469–478.
- [7] Yao, X., P. Qin, and J. Guan. Residual mechanical properties and constitutive model of high-strength seismic steel bars through different cooling rates. *Materials*, Vol. 14, No. 2, 2021, pp. 469–477.
- [8] Zhang, D., W. Huang, and J. Zhang. Prediction of fatigue damage in ribbed steel bars under cyclic loading with a magneto-mechanical coupling model. *Journal of Magnetism and Magnetic Materials*, Vol. 530, 2021, id. 167943.
- [9] Zong, Z., S. Kunnath, and G. Monti. Simulation of Reinforcing Bar Buckling in Circular Reinforced Concrete Columns. ACI Structural Journal, Vol. 110, No. 4, 2013, pp. 607–616.

- [10] Li, D., C. Xiong, and T. Huang. A simplified constitutive model for corroded steel bars. *Construction and Building Materials*, Vol. 186, 2018, pp. 11–19.
- [11] Fernandez, I., J. M. Bairán, and A. R. Marí. Corrosion effects on the mechanical properties of reinforcing steel bars. Fatigue and  $\sigma$ - $\epsilon$  behavior. *Construction and Building Materials*, Vol. 101, 2015, pp. 772–783.
- [12] Abdalla, J. A. and R. A. Hawileh. Artificial neural network predictions of fatigue life of steel bars based on hysteretic energy. *Journal of Computing in Civil Engineering*, Vol. 27, No. 5, 2013, pp. 489–496.
- [13] Chou, P. Y., J. T. Tsai, and J. H. Chou. Modeling and optimizing tensile strength and yield point on a steel bar using an artificial neural network with Taguchi particle swarm optimizer. *IEEE Access*, Vol. 4, 2016, pp. 585–593.
- [14] Zhang, Y. T., B. G. Zhao, and R. G. Li. Monotonic and low cycle fatigue testing and research for HRB400 steel. *Engineering Mechanics*, Vol. 33, No. 4, pp. 121–129 (in Chinese).
- [15] Xu, Q. Y., Z. Y. Fang, and Q. T. Lin. Comparative experimental study of fatigue performance of HRB500 and HRB400 reinforcing bar. *Journal of Experiments Mechanics*, Vol. 34, 2019, pp. 105–112 (in Chinese).
- [16] Gao, L., C. Sun, and M. L. Zhuang. Fatigue life prediction of HTRB630E steel bars based on modified coffin-manson model under pre-strain. *Structures*, Vol. 38, 2022, pp. 28–39.
- [17] Han, Q., M. Hu, and K. Xu. Hysteretic behavior and modelling of ultra-high-strength steel bar including buckling. *Bulletin of Earthquake Engineering*, Vol. 17, 2019, pp. 5265–5289.
- [18] National standards of People's Republic of China. *Metallic materials- Tensile tests-Part 1: Test methods at room temperature GB/T228.1-2010*, Standards Press of China, Beijing, 2010 (in Chinese).
- [19] Jiangsu Tianshun Metal Materials Group Co., Ltd. and School of Civil Engineering in Southeast University. Jiang Su JG/T 054-2012 Technical Specification for Heat-treated Ribbed High-strength Reinforced Concrete Structures, Jiangsu Science and Technology Press, Nanjing, 2012 (in Chinese).
- [20] Brown, J. and S. K. Kunnath. Low cycle fatigue behavior of longitudinal reinforcement in reinforced concrete bridge columns. *Technical Report MCEER*, Vol. 7, 2000, pp. 109–109.
- [21] Sivaprasad, S., S. K. Paul, and A. Das. Cyclic plastic behaviour of primary heat transport piping materials: Influence of loading schemes on hysteresis loop. *Materials Science and Engineering: A*, Vol. 527, No. 26, 2010, pp. 6858–6869.
- [22] Michael, H. S. Uniaxial Material Command. OpenSees. Accessed on 20 Nov. 2023. https://opensees.berkeley.edu/wiki/index.php/ UniaxialMaterial\_Command.
- [23] Chang, G. A. and J. B. Mander. Seismic energy based fatigue damage analysis of bridge columns: Part I-Evaluation of seismic capacity, National Center for Earthquake Engineering Research, Buffalo, NY, 1994.
- [24] Kunnath, S. K., Y. A. Heo, and J. F. Mohle. Nonlinear uniaxial material model for reinforcing steel bars. *Journal of Structural Engineering*, Vol. 135, No. 4, 2009, pp. 335–343.
- [25] Mander, J. B. Seismic design of bridge piers. Doctor's thesis, University of Canterbury, Christchurch, 1984.
- [26] Ministry of Housing and Urban-Rural Development of the People's Republic of China. Code for design of concrete structures. GB50010-2010, China Standard Press, Beijing, 2010 (in Chinese).
- [27] Wei, Y. Inelastic modeling of reinforcing bars and blind analysis of the benchmark tests on beamcolumn joints under cyclic loading. Doctor's thesis. Università degli Studi di Pavia, 2006.

- [28] Wang, M. Damage and degradation behavior of steel frames under severe earthquake, Doctor's thesis, Tsinghua University, 2013 (in Chinese).
- [29] Menegotto, M. Method of analysis for cyclically loaded RC plane frames including changes in geometry and non-elastic behavior of elements under combined normal force and bending. Proc. of IABSE Symposium on Resistance and Ultimate Deformability of Structures Acted on by Well Defined Repeated Loads, 1973.
- [30] Filippou, F. C., E. P. Popov, and V. V. Bertero. Effects of bond deterioration on hysteretic behavior of reinforced concrete joints, College of Engineering University of California, 1983.
- [31] Chang, G. A., and J. B. Mander. Seismic energy based fatigue damage analysis of bridge columns: Part II-evaluation of seismic demand. National Center for Earthquake Engineering Research. 1994.
- [32] Zhang, Y. T., B. K. Zhao, and R. Q. Li. Monotonic and low cycle fatigue testing and research for HRB400 steel. *Engineering Mechanics*, Vol. 33, No. 4, 2016, pp. 121–129.
- [33] Sun, C. Z., C. Q. Miao, and A. Q. Li. Experimental study on low cycle fatigue properties of 630 MPa super-high strength steel bar. *Journal of Building Structures*, Vol. 4, No. 4, 2019, pp. 194–202.

- [34] Gomes, A. and J. Appleton. Nonlinear cyclic stress-strain relationship of reinforcing bars including buckling. *Engineering Structures*, Vol. 19, No. 10, 1997, pp. 822–826.
- [35] Lowes, L. N. and A. Altoontash. Modeling the response of reinforced concrete beam-column joints. *Journal of Structural Engineering*, Vol. 17, No. 8, 2002, pp. 1686–1697.
- [36] Nilinjan, M. Pinching4 Material. https://opensees.berkeley.edu/wiki/ index.php/Pinching4 Material. University of Washington.
- [37] Michael, S. *Hysteretic Material*. https://opensees.berkeley.edu/wiki/index.php/Hysteretic Material Oregon State University.
- [38] Wu, D., Y. Ding, and J. Su. Investigation on low-cycle fatigue performance of high-strength steel bars including the effect of inelastic buckling. *Engineering Structures*, Vol. 272, 2022, id. 114974.
- [39] Gibbons, J. D., S. Chakraborti. Nonparametric statistical inference: Revised and expanded, CRC Press, 2014.
- [40] He, L., B. Agard, and M. Trépanier. A classification of public transit users with smart card data based on time series distance metrics and a hierarchical clustering method. *Transportmetrica A: Transport Science*, Vol. 16, No. 1, 2020, pp. 56–75.
- [41] Reshef., D. N., Y. A. Reshef, and H. K. Finucane. Detecting novel associations in large data sets. *Science*, Vol. 334, No. 6062, 2011, pp. 1518–1524.